Original Article

Full-length dystrophin deficiency leads to contractile and calcium transient defects in human engineered heart tissues

Journal of Tissue Engineering
Volume 13: 1–16

DOI: 10.1177/20417314221119628
journals.sagepub.com/home/tej
SAGE

Samantha B Bremner[1,2], Christian J Mandrycky[1,2], Andrea Leonard[2,3,4], Ruby M Padgett[2,3,4], Alan R Levinson[1], Ethan S Rehn[1], J Manuel Pioner[5], Nathan J Sniadecki[1,2,3,4,6] and David L Mack[1,2,7]

Abstract

Cardiomyopathy is currently the leading cause of death for patients with Duchenne muscular dystrophy (DMD), a severe neuromuscular disorder affecting young boys. Animal models have provided insight into the mechanisms by which dystrophin protein deficiency causes cardiomyopathy, but there remains a need to develop human models of DMD to validate pathogenic mechanisms and identify therapeutic targets. Here, we have developed human engineered heart tissues (EHTs) from CRISPR-edited, human induced pluripotent stem cell-derived cardiomyocytes (hiPSC-CMs) expressing a truncated dystrophin protein lacking part of the actin-binding domain. The 3D EHT platform enables direct measurement of contractile force, simultaneous monitoring of Ca^{2+} transients, and assessment of myofibril structure. Dystrophin-mutant EHTs produced less contractile force as well as delayed kinetics of force generation and relaxation, as compared to isogenic controls. Contractile dysfunction was accompanied by reduced sarcomere length, increased resting cytosolic Ca^{2+} levels, delayed Ca^{2+} release and reuptake, and increased beat rate irregularity. Transcriptomic analysis revealed clear differences between dystrophin-deficient and control EHTs, including downregulation of genes related to Ca^{2+} homeostasis and extracellular matrix organization, and upregulation of genes related to regulation of membrane potential, cardiac muscle development, and heart contraction. These findings indicate that the EHT platform provides the cues necessary to expose the clinically-relevant, functional phenotype of force production as well as mechanistic insights into the role of Ca^{2+} handling and transcriptomic dysregulation in dystrophic cardiac function, ultimately providing a powerful platform for further studies in disease modeling and drug discovery.

Keywords

Duchenne muscular dystrophy, engineered heart tissue, human induced pluripotent stem cell-derived cardiomyocytes, disease modeling

Date received: 2 June 2022; accepted: 28 July 2022

[1]Department of Bioengineering, University of Washington, Seattle, WA, USA
[2]Institute for Stem Cell and Regenerative Medicine, University of Washington, Seattle, WA, USA
[3]Department of Mechanical Engineering, University of Washington, Seattle, WA, USA
[4]Center for Cardiovascular Biology, University of Washington, Seattle, WA, USA
[5]Department of Biology, University of Florence, Florence, Italy
[6]Department of Laboratory Medicine and Pathology, University of Washington, Seattle, WA, USA
[7]Department of Rehabilitation Medicine, University of Washington, Seattle, WA, USA

Corresponding authors:
Nathan J Sniadecki, Department of Mechanical Engineering, University of Washington, 850 Republican Street, Box 358056, Seattle, WA 98109, USA.
Email: nsniadec@uw.edu

David L Mack, Department of Rehabilitation Medicine, University of Washington, 850 Republican Street, Box 358056, Seattle, WA 98109, USA.
Email: dmack21@uw.edu

Introduction

Duchenne muscular dystrophy (DMD) is characterized by profound skeletal muscle weakness and wasting, but the leading cause of death in these patients is congestive heart failure downstream of dilated cardiomyopathy.[1] DMD and Becker muscular dystrophy (BMD), the less severe form of the disease, are caused by a lack of full-length dystrophin, a long, rod-shaped protein that localizes to the sarcolemma, where it anchors the sarcolemma to the extracellular matrix and the intracellular cytoskeleton through recruitment of the dystroglycan complex.[2] Dystrophin deficiency causes increased cell fragility and vulnerability to contraction-induced cell damage, leading to cycles of cardiac degeneration along with a gradual accumulation of non-contractile fibrotic tissue as the disease progresses.[3] Lack of dystrophin also has pleiotropic effects on cardiomyocyte function, including Ca^{2+} dysregulation,[4,5] nitric oxide dysregulation,[6,7] and mitochondrial dysfunction,[8,9] leading to oxidative damage and cell death.[10,11] Dystrophin expression first occurs early in cardiac development,[12,13] thus, a lack of functional dystrophin likely affects cardiac development well before the presentation of clinical symptoms.[14,15] However, the cellular mechanisms by which dystrophin deficiency leads to cardiac dysfunction at the organ level are not well understood, further complicated by limitations of current disease models. As such, the development of improved human in vitro disease models would be of great benefit to the field.

Current models are insufficient to fully elucidate the mechanisms of cardiomyopathy progression in DMD, as commonly used animal models have only mild and late-onset cardiac phenotypes and fail to recapitulate the human condition. The *mdx* mouse,[16] although relied upon heavily to advance our understanding of DMD, displays a minimal reduction in average lifespan when compared to human patients and presents minimal disease phenotypes or clinical indicators of cardiomyopathy until much later in disease progression.[17,18] This lack of clinically relevant symptoms is often accompanied by spontaneous rhabdomyosarcoma, something not seen in human DMD patients.[19] Larger animal models, while often presenting more severe disease phenotypes, are limited by disease phenotype variability, high maintenance costs, and ultimately, a lack of relevant human physiology.[20] Additionally, given ethical concerns surrounding the use of animal in research, there is a desire to reduce and replace the use of animal models. Hence, there exists a need for human models of DMD suitable for preclinical studies to validate the molecular drivers of cardiac and skeletal muscle pathology and test genetic and small molecule therapeutics quickly and inexpensively.

Human induced pluripotent stem cell-derived cardiomyocytes (hiPSC-CMs) have emerged as a useful tool to study the multiple facets of dystrophin function not easily explored with animal models.[21] These stem cell-derived models have successfully replicated many known dystrophic phenotypes observed in DMD patients, including membrane fragility, Ca^{2+} handling and electrophysiological abnormalities, mitochondrial damage, and impaired force production.[21–30] However, hiPSC-CMs grown in 2D tissue culture platforms are limited by an immature cardiac phenotype, requiring long-term culture or a combination of structural and biochemical cues to promote sufficient maturation and accentuate the multifaceted dystrophic phenotype.[23,31] These 2D platforms also subject cells to non-physiologic culture conditions and rely on single-cell measures, all of which limit the ability to capture an accurate and complete representation of cardiac function in both the normal and diseased states. 3D cardiac tissue engineering holds promise to produce models that more accurately mimic dystrophic cardiomyopathy in vitro.

We have previously developed engineered heart tissues (EHTs) that provide a 3D, physiological cell culture platform that allows for the assessment of hiPSC-CM auxotonic contractile function under uniaxial tensile load.[32–34] The EHT platform consists of hiPSC-CMs and stromal cells suspended in a fibrin hydrogel between two silicone posts, one flexible and one rigid, that forms synchronously contracting tissues, allowing for measurement of contractile force and kinetics. EHTs promote uniaxial cell alignment and physiological auxotonic contractions, which has been shown to improve cardiac maturation beyond what is achieved in 2D culture.[35–39] We hypothesize that the EHT platform will provide the environment necessary to expose the structural and physiological differences between normal and dystrophin-deficient heart muscle in vitro.

In this study, we generated EHTs from genetically-edited hiPSC-CMs harboring a dystrophin-truncating mutation (DMD 263delG).[31,40] Compared to isogenic controls, we observed that DMD 263delG EHTs display reduced contractile force and delayed kinetics of force development and relaxation. This was observed in addition to impaired sarcomere development, as dystrophic EHTs were found to have shorter sarcomere lengths. Dystrophic EHTs were also found to have increased cytosolic Ca^{2+} levels, slowed Ca^{2+} transient kinetics, and a higher incidence of irregular beat intervals as compared to isogenic controls. Transcriptome sequencing indicated dysregulation of several biological processes in DMD 263delG EHTs, including those related to heart development and contraction, Ca^{2+} and membrane potential homeostasis, and organization of the extracellular matrix. These results demonstrate that the EHT platform provides sufficient maturational cues to expose multiple facets of the DMD phenotype in a single platform. The results of this and future studies will continue to uncover and refine our understanding of the mechanisms by which dystrophin deficiency leads to heart failure early in disease

progression and provide a platform for testing new genetic and small molecule therapies.

Materials and methods

Stem cell culture and directed cardiac differentiation

A urine-derived hiPSC line from a healthy male donor (control) was established as previously described.[22] An isogenic diseased cell line harboring a dystrophin mutation (DMD 263delG) was generated from the control cell line via the deletion of a single base pair in exon 1 of the DMD gene with CRISPR-Cas9 as previously described.[31] Undifferentiated hiPSCs were maintained in mTeSR1 (Stemcell Technologies) on tissue culture plates coated with a 1:60 dilution of Matrigel (Corning). Cardiomyocyte directed differentiation was performed using a modified small molecule Wnt-modulating protocol optimized to each cell line as previously described.[41] Briefly, hiPSCs were seeded at $1.5–2.5 \times 10^5$ cells/cm^2 on Matrigel-coated plates in mTeSR1 with 10 μM Y-27632 ROCK inhibitor (Tocris). Cells were maintained in mTeSR1 with daily media changes until they reached confluency, which was typically 2–3 days after initial seeding. The initiation of directed differentiation (day 0) was defined by changing the media to RPMI 1640 (Gibco) plus B-27 supplement minus insulin (Life Technologies) and 12–14 μM Chiron 99021 (Axon Medchem) to activate Wnt/β-catenin signaling via inhibition of glycogen synthase kinase-3β (GSK-3β). After 24 h (day 1), media was changed to RPMI with B-27 minus insulin. On day 3, media was changed to RPMI with B-27 minus insulin and 5 μM IWP-4 (Stemgent) to inhibit Wnt/β-catenin signaling. On day 5, media was changed to RPMI with B-27 minus insulin. On day 7, the media was changed to RPMI with B-27 supplement (with insulin) and media was subsequently changed every 2–3 days. All differentiation steps were performed in 12-well plates with media volumes of 2 mL per well. hiPSC-CMs were replated into 10 cm dishes on day 14 to prepare for lactate enrichment. On days 16 and 18, media was changed to DMEM without glucose (Gibco) supplemented with 4 mM sodium L-lactate (Sigma-Aldrich) to enrich for cardiomyocytes. Cells were returned to RPMI with B-27 supplement plus insulin and cultured until day 25–27. Prior to EHT casting, cardiomyocyte purity ($> 90\%$) was evaluated by flow cytometry for cardiac troponin T (Supplemental Figure S1). All cell culture media was supplemented with 100 U/mL penicillin-streptomycin.

EHT platform and tissue casting

The EHT post platform was designed and fabricated as described previously, resulting in racks of six pairs of posts measuring 12 mm long and 1.5 mm in diameter with a cap.[32–34] Briefly, uncured polydimethylsiloxane (PDMS, Sylgard 184 mixed at a 10:1 ratio of base to curing agent) was poured into a four-part acrylic mold with a glass capillary tube (Drummond, Cat #1-000-0500) inserted into one post of each pair to make it rigid. Posts were left to cure at room temperature for 24 h then baked at 65 °C overnight to cure completely before being separated from the mold. Prior to EHT casting, PDMS posts were submerged in 70% ethanol for 10 min, rinsed with sterile deionized water for 10 min, then UV sterilized for 10 min. The PDMS had a modulus of elasticity of 2.5 MPa, so the bending stiffness of the flexible post in each pair was calculated to be 0.95 μN/μm, as previously described.[32,42]

EHTs were cast on day 25–27 of cardiac differentiation as previously described.[33,34] Briefly, rectangular 2% agarose casting molds were prepared in 24-well tissue culture plates using 3D-printed spacers. Each rack of PDMS posts was positioned upside down with the tips of posts centered in the agarose wells. A solution of 100 μL volume consisting of 7.5×10^5 hiPSC-CMs and 5×10^4 HS27a human bone marrow stromal cells (ATCC) in RPMI with B-27 with 5 mg/mL bovine fibrinogen (Sigma-Aldrich) and 3 U/mL thrombin (Sigma-Aldrich) was pipetted into each agarose well. The mixture was incubated at 37 °C for 80 min to form EHTs suspended between pairs of posts and then transferred into a new 24-well plate with EHT media (RPMI with B-27 supplemented with 5 mg/mL aminocaproic acid, Sigma-Aldrich) for culture. EHT media was exchanged every 2–3 days for 3 weeks before subsequent analysis.

Contractile force measurement

EHTs were placed in a Tyrode's buffer (1.8 mM $CaCl_2$, 1 mM $MgCl_2$, 5.4 mM KCl, 140 mM NaCl, 0.33 mM NaH_2PO_4, 5 mM glucose, pH 7.35) at 37 °C for contractile analysis. A custom pacing apparatus with carbon electrodes built to fit a 24-well plate was used with an electrical stimulator (Astro Med Grass Stimulator, Model S88X) to provide biphasic field stimulation at 1.5 Hz (5 V/cm for 10 ms duration) during imaging.[33] Videos of EHT contraction were taken at 66.7 frames/s using an ORCA-Flash4.0 C13440 CMOS camera (Hamamatsu) on a Nikon TEi epifluorescent microscope with a 2× objective and 0.7× coupler, providing 4.64 μm/pixel resolution and a field of view of 9.5 mm × 9.5 mm, which was sufficient to visualize the full length of the EHTs and the tips of both posts. A custom MATLAB script was used to track the deflection of the flexible post relative to the rigid post and from this analysis, we calculated twitch force, shortening velocity, time to peak, time to 50% and 90% relaxation, active twitch power, and total twitch work, as previously described.[42,43] Briefly, twitch force was calculated by subtracting the tissue force minima from the following maxima and contraction kinetic metrics were calculated from the unnormalized tissue force traces. Shortening velocity was calculated as

the maximum derivative of tissue force of each EHT contraction. EHT cross-sectional area was calculated assuming an elliptical cross section with a measured tissue width and conservatively estimated thickness of 500 μm. Specific force was then calculated by dividing the twitch force of each EHT by its cross-sectional area. For each EHT, analysis was performed on five consecutive contractions.

Beat interval irregularity measurement

Before initiation of electrical pacing, video recordings of spontaneously beating EHTs were taken to assess beat rate variability as previously described.[23,44] Briefly, EHTs were submerged in Tyrode's buffer at 37 °C and a video of the flexible post was recorded for 60 s at 10 frames/s during spontaneous contraction. Post deflection was tracked and beat intervals (BI) were measured using a custom MATLAB script. BI were identified using a noise tolerant, peak finding algorithm that identifies local maxima that are greater than a threshold of one-fourth the amplitude of the data above the minimum. BI irregularity (ΔBI) was calculated as the difference between subsequent BI ($\Delta BI = BI_{n+1} - BI_n$).

Ca^{2+} transient measurement

Ca^{2+} transients in EHTs were assessed using the ratiometric Ca^{2+} indicator dye Fura-2 AM (Invitrogen), under 1.5 Hz electrical stimulation in Tyrode's buffer at 37 °C. To load Fura-2, EHTs were incubated in EHT media with 5 μM Fura-2 AM for 1 h followed by a washout period of 30 min in EHT media before being transferred to Tyrode's buffer. Two custom filter cubes (Chroma) were used to excite the dye at 365 nm or 380 nm and capture its emission at 510 nm. Excitation at 365 nm is near the isosbestic point of Fura-2 (360 nm) while emission intensity with 380 nm excitation decreases with increasing Ca^{2+} levels. Videos were taken at 50 frames/s on an ORCA-Flash4.0 C13440 CMOS camera (Hamamatsu) on a Nikon TEi epifluorescent microscope with a 2× objective and 0.7× coupler as described. To enable ratiometric Ca^{2+} assessment, a series of three videos of EHT contraction were taken sequentially at 365 nm, 380 nm, and again at 365 nm excitation. These videos were then analyzed with a custom MATLAB script to track the position of the flexible post and determine the average pixel intensity within the EHT area during contraction. The fluorescence intensity of the two 365 nm excitation recordings at the start and end of the experiments were averaged to account for any effects of photobleaching of the dye. The average was then used in calculating a ratio of baseline fluorescence intensity at 365 nm excitation over the dynamic fluorescence intensity at 380 nm excitation due to changes in the concentration of intracellular Ca^{2+}. The 365 nm/380 nm ratio was then used to calculate the kinetics of the Ca^{2+} transient, including time to peak, time to 50% decay, and rate to 50% decay. For each EHT, analysis was performed on 5 consecutive contractions.

Immunoblot

Protein lysates were obtained from a subset of individual EHTs after force and Ca^{2+} measurements using an ice-cold RIPA buffer supplemented with 2% protease inhibitor cocktail (Sigma P8340). Individual EHTs were homogenized in 75–100 μL of buffer using a micro-homogenizer with a 5 mm probe (VWR). Samples were lysed on ice for 30 min, then spun down at 21,000*g* for 10 min at 4 °C to remove cellular and matrix debris. The supernatant was isolated and protein concentration was measured using the Pierce BCA Protein Assay Kit (Thermo Fisher Scientific) according to manufacturer's instructions.

Samples were prepared for electrophoresis by adding 4× Laemmli Sample Buffer (Bio-Rad) and 2.5% β-mercaptoethanol, after which samples were denatured at 95 °C for 10 min. Protein was loaded into 4–15% Mini-PROTEAN TGX Stain-Free Gel at 50 μg per sample and run at 100 V for 80 min in 1× Tris/Glycine/SDS running buffer (Bio-Rad). Protein gels were transferred onto Immun-Blot LF PVDF membranes (Bio-Rad) overnight at 30 V and 4 °C in 1× Tris/Glycine buffer (Bio-Rad) with 10% methanol. Membranes were blocked in Blocker FL Fluorescent Blocking Buffer (Thermo Fisher Scientific) for 1 h at room temperature. Primary antibodies against dystrophin (Abcam 15277, 1:1000), β-dystroglycan (DSHB MANDAG2(D11), 1:1000), and GAPDH (Sigma SAB4300645, 1:1000) were diluted in blocking buffer and incubation was performed overnight at 4 °C with agitation. Membranes were washed three times for 5 min in TBS-T at room temperature, then incubated for 1 h at room temperature with species-matched AlexaFluor-conjugated secondary antibodies (Invitrogen, 1:1000) diluted in blocking buffer with agitation. Membranes were again washed three times for 5 min in TBS-T before imaging on a ChemiDoc MP imaging system (Bio-Rad). Before re-probing for other targets, membranes were stripped of antibodies with Restore Plus Western Stripping Buffer (Thermo Fisher Scientific) for 10 min, then washed 3 times for 10 min in TBS-T at room temperature. Densitometric quantification of western blot band intensity was performed using ImageJ and protein levels were normalized to the level of GAPDH in the sample.

Immunofluorescent imaging and quantitative sarcomere analysis

A subset of EHTs were processed for histology as previously described.[33] Briefly, following force and Ca^{2+} assessment, EHTs were submerged in 140 mM KCl for 1 min to inhibit contraction and induce EHT relaxation followed by fixation in 4% paraformaldehyde in DPBS for 15 min. EHTs were then washed with DPBS and

dehydrated in a 30% w/v sucrose solution overnight at 4 °C. EHTs were removed from the posts and embedded in O.C.T. compound. Longitudinal and transverse cryosections of 20 µm thickness were used for histology. Sections were blocked and permeabilized with 1% BSA and 0.1% Triton X-100 for 30 min at room temperature, followed by overnight incubation at 4 °C with mouse primary antibodies against α-actinin (Sigma-Aldrich A7811, 1:800) or dystrophin (Leica NCL-DYS1 (monoclonal, 1:30) or Abcam 15277 (polyclonal, 1:200). The following day, sections were incubated with donkey anti-mouse Alexa Fluor 488, donkey anti-rabbit Alexa Fluor 555, or goat anti-mouse Alexa Fluor 594 (Invitrogen, 1:200), and Alexa Fluor 488 phalloidin (Invitrogen A12379, 1:150), for 1 h at room temperature. Cover slides were mounted with ProLong™ Gold Antifade Mountant with DAPI (Invitrogen). Images were taken on a Leica SP8 confocal microscope. Laser strength and gain were kept constant between all samples and fields of view. Resting sarcomere length and alignment were calculated using α-actinin stained images and a scanning gradient Fourier transform program in MATLAB, as previously described.[45] Z-disk width was calculated using a custom MATLAB script that thresholds and measures the major axis length of α-actinin stained images. Dystrophin stain intensity was quantified by applying a threshold mask to images to select cell area then averaging the pixel intensity within the mask.

RNA sequencing

Following force and Ca^{2+} assessments, a subset of EHTs were removed from posts and stored in RNAlater (Ambion) at −80°C. Lactate enriched, age-matched hiPSC-CMs (7 weeks post differentiation) were similarly stored in RNAlater at −80°C. Individual EHTs and hiPSC-CM samples were sent to BGI genomics for RNA extraction and 100 base pair paired-end transcriptome sequencing on the DNBseq platform with 50 million reads per sample. Reads were aligned to the human genome using Rsubread (Bioconductor) to GENCODE GRCh38.p13.[46] Aligned reads were then counted using featureCounts (Bioconductor), excluding chimeras, multi-mapping genes, multi-overlap, and single end genes, resulting in roughly 20 million counts per individual EHT.[46] Differential expression analysis was performed using edgeR (Bioconductor) and the following criteria: counts > 10, $p < 0.05$, $|\log(FC)| > 0.3$, FDR < 0.05.[47] Gene ontology (GO, 02/2021 release) analysis was performed with clusterProfiler (Bioconductor).[48]

Biological replicates and statistical analysis

The data shown herein represent EHTs pooled from multiple experimental replicates as indicated, where an independent experiment refers to a batch of EHTs made from an independent differentiation. The data encompasses up to three independent experiments with 6–12 tissues per batch, as indicated in figure legends. All data points shown in figures represent values for a single EHT and different symbols designate separate experiments. All values are reported as mean ± standard error of the mean (S.E.M.) unless indicated otherwise. Results were compared using an unpaired, two-tail t-test unless indicated otherwise and differences with a p-value < 0.05 were considered statistically significant as denoted with an asterisk.

Results

Generation of EHTs from dystrophin-mutant hiPSC-CMs

Control hiPSCs were generated from urine derived cells from a healthy donor as previously described.[22] The control line was genetically edited using CRISPR-Cas9 to generate an isogenic match that harbored a dystrophin-truncating mutation (DMD 263delG).[31,40] Briefly, the DMD 263delG line has a single base pair deletion within the first exon of the *DMD* gene, resulting in the expression of a truncated isoform of dystrophin lacking a significant portion of the actin-binding domain (exons 1–6) (Figure 1(a)). N-terminal *DMD* mutations are known to cause more severe cases of Becker's muscular dystrophy.[49] Both control and DMD 263delG hiPSCs were subjected to directed cardiomyocyte differentiation and used to generate EHTs by casting hiPSC-CMs in a fibrin gel between two silicone posts, one flexible and one rigid (Figure 1(b)). Both control and DMD 263delG hiPSC-CMs generated EHTs that compacted in size between the posts and began to generate observable spontaneous contractions within 1 week of casting (Figure 1(c)). Both control and DMD hiPSC-CMs produced EHTs of similar resting length and cross-sectional area, indicating that EHT compaction, and therefore resting tissue force and stress, was consistent between the two lines (Supplemental Figure S2). Western blot analysis using a polyclonal antibody against the C-terminal domain of dystrophin showed similar expression levels of dystrophin protein in control and DMD 263delG EHTs (Figure 1(d) and (e), Supplemental Figure S4). Additionally, we observed lower-trending expression of β-dystroglycan, another dystroglycan complex protein, in DMD 263delG EHTs (Figure 1(d) and (e), Supplemental Figure S4), recapitulating the most recent demonstration of dystroglycan protein complex assembly in hiPSC-CMs.[50] However, while immunocytochemical analysis of sarcomeric F-actin confirmed the presence of uniaxially aligned sarcomeres in control and DMD 263delG EHTs, an antibody targeting the rod domain of dystrophin (exons 26–30) indicated a high amount of the full-length protein in the control EHTs and only a trace amount of the truncated protein in the DMD 263delG EHTs (Figure 1(f), Supplemental Figure S3). Similarly, in transverse sections, we observed that dystrophin localized strongly to the cell membrane in control EHTs, while less dystrophin appeared

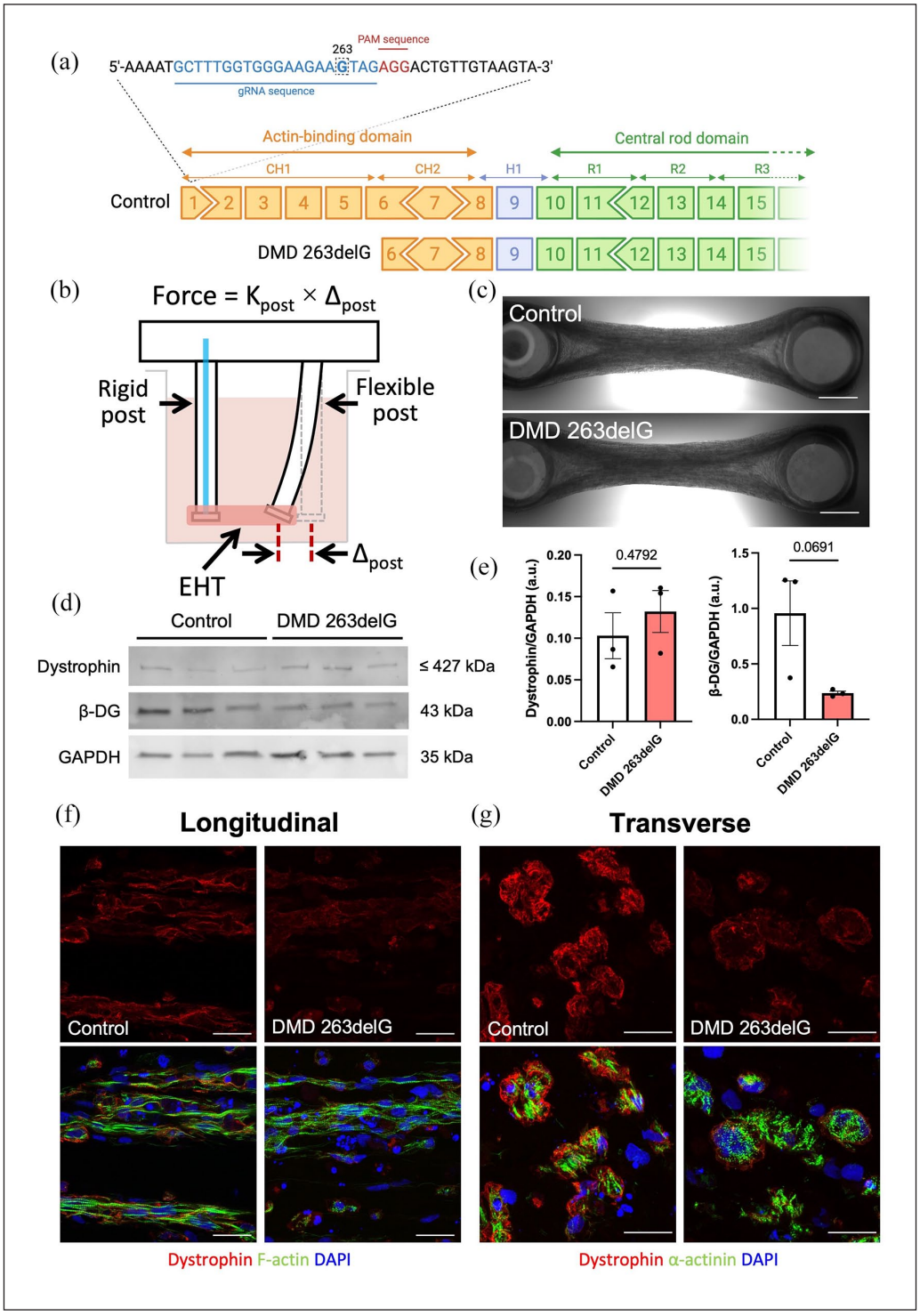

Figure 1. Human engineered heart tissues as a model of DMD. (a) Schematic of the CRISPR gene editing strategy that targeted the first exon of the *DMD* gene, resulting in the deletion of G263 to generate the DMD 263delG cell line which expresses a truncated protein missing the actin-binding domain up to exon 6. (b) Schematic diagram showing an EHT attached to two posts, one flexible and one rigid, in culture. The force of EHT contraction can be quantified using the stiffness (K_{post}) and measured deflection (Δ_{post}) of the flexible post. (c) Representative images of control DMD 263del EHTs with the rigid post on the left and the flexible post on the right. Scale bars = 1 mm. (d) Western blot analysis of dystrophin and β-dystroglycan (β-DG) expression in individual control and DMD 263delG (DMD) EHTs, with GAPDH as a loading control ($n = 3$). (e) Normalized protein level of dystrophin and β-dystroglycan based on loading control GAPDH ($n = 3$, p-values indicated). (f) Immunofluorescent images of longitudinal EHT sections stained for dystrophin (Leica NCL-DYS1, red), F-actin (Phalloidin, green), and nuclei (DAPI, blue). Scale bars = 50 µm. (g) Immunofluorescence images of transverse sections of control and DMD 263delG EHTs stained with a polyclonal antibody for dystrophin (Abcam 15277, red), α-actinin (green), and nuclei (blue). Scale bars = 25 µm.

at the cell membrane in DMD 263delG EHTs (Figure 1(g)). Together, these results suggest that while there was equivalent total expression of dystrophin in the DMD 263delG EHTs as seen by western blot, there was decreased localization of this truncated dystrophin to the cell membrane as seen by immunofluorescence. The observed decrease in β-dystroglycan expression further supports this hypothesis of impaired dystroglycan protein complex formation in the absence of full-length dystrophin.

Transcriptional phenotype of DMD hiPSC-CMs and EHTs

We performed RNA-sequencing on age-matched hiPSC-CMs and EHTs to investigate the transcriptomic effects of 3D EHT culture downstream of the DMD 263delG mutation (Figure 2(a)). We observed that 2D cell culture produced more differentially expressed genes (DEGs, $|\log(FC) > 0.3|$, $p < 0.05$, FDR < 0.05, $n = 3$) between control and DMD 263delG samples than EHTs (4233 DEGs for 2D cell culture versus 1527 DEGs for EHTs) (Figure 2(b)). Interestingly, there appeared to be very little overlap between DEGs upregulated or downregulated as a result of the DMD 263delG mutation in 2D cell culture when compared to EHTs. To better demonstrate the differences between 2D and EHT culture, we compared the top 30 upregulated and downregulated gene ontology (GO) biological processes (BP) as ranked by *p*-value (Figure 2(c) and (d)). When comparing 2D control and DMD 263delG hiPSC-CMs, very little emerges that is relevant to dystrophin function or cardiac biology. Interestingly, while there was a downregulation of genes related to heart development and cardiac muscle cell action potential, the majority of BP terms relate to a large upregulation in mitochondrial function and ATP generation, with downregulation of BPs related to neural development, epithelial morphogenesis, and hemostasis (Figure 2(c)). Conversely, when comparing control and DMD 263delG EHTs, we observed dysregulation of many BPs relevant to cardiac function, including many related to heart and cardiac muscle development, cardiac action potential and muscle contraction, as well as extracellular matrix organization (Figure 2(d)). These results suggest that the *DMD* 263delG mutation does not have a profound effect on the cardiac-specific transcriptome in 2D culture, perhaps due to decreased hiPSC-CM maturity in this less physiologically-relevant culture platform, while the uniaxial, 3D culture provided by EHTs produces a disease-relevant transcriptomic response.

A closer analysis of the transcriptional changes that occurred in DMD 263delG EHTs reveals potential mechanisms driving the dystrophic phenotype presented in EHTs. Direct comparison of a subset of DEGs with the highest fold change revealed a hierarchical clustering that clearly delineates the two genotypes (Figure 2(e)). GO analysis indicated dysregulation of several key BPs including those related to cardiac muscle tissue development, heart contraction, regulation of membrane potential, calcium ion homeostasis, and extracellular matrix organization (Figure 2(f)). Further inspection of key genes identified by GO analysis indicates potential drivers of the dystrophic phenotype presented in EHTs (Supplemental Table S1). Interestingly, we observed increased expression of *DMD* mRNA in DMD 263delG EHTs, potentially indicating an attempted compensatory mechanism for the dysfunctional mutant dystrophin protein. Ultimately, we observed that 3D EHT culture produces transcriptional changes relevant to cardiac biology, suggesting multiple mechanisms driving the dystrophic phenotype produced as a result of a lack of full-length dystrophin.

Decreased contractility and delayed contractile kinetics in DMD EHTs

Given the central role of dystrophin in maintaining mechanical integrity of the cell, it was of interest to assess the extent to which dystrophic EHTs are able to produce contractile forces. After 3 weeks in culture, control and DMD 263delG EHTs were subjected to auxotonic contractility assessment with electrical field stimulation at 1.5 Hz via optical measurement of the deflection of the flexible post. It was observed that DMD 263delG EHTs had a similar baseline tension as control EHTs but produced significantly decreased twitch forces (Figure 3(a) and (b)). Accordingly, DMD 263delG EHTs produced lower specific forces than the control EHTs when estimated cross-sectional areas were accounted for (Figure 3(c)). DMD 263delG EHTs were also observed to have lower twitch power, twitch work, and shortening velocity, as compared to control EHTs, illustrating an overall decrease in contractile performance (Figure 3(d)–(f)). Normalized traces of tissue force (Figure 3(g)) reveal slower kinetics of contraction in DMD 263delG EHTs, which significantly increased the time to peak force and time to 50% relaxation (Figure 3(h)–(j)). All representative tissue traces are shown in Supplemental Figure S5. Overall, these results indicate that the dystrophin mutation results in impaired contractile function in DMD 263delG EHTs.

Altered sarcomere structure in DMD EHTs

To investigate the underlying causes of impaired contractility, we performed quantitative image analysis of myofibril structure. Specifically, control and DMD 263delG EHTs were stained for Z-disk protein α-actinin, and confocal images were analyzed with custom image analysis scripts. We observed that both the control and DMD 263delG EHTs generated cardiomyocytes that had sarcomeres aligned in the longitudinal direction (Figure 4(a)). Sarcomere length was quantified using a scanning-gradient Fourier transform.[45] We found that control EHTs had

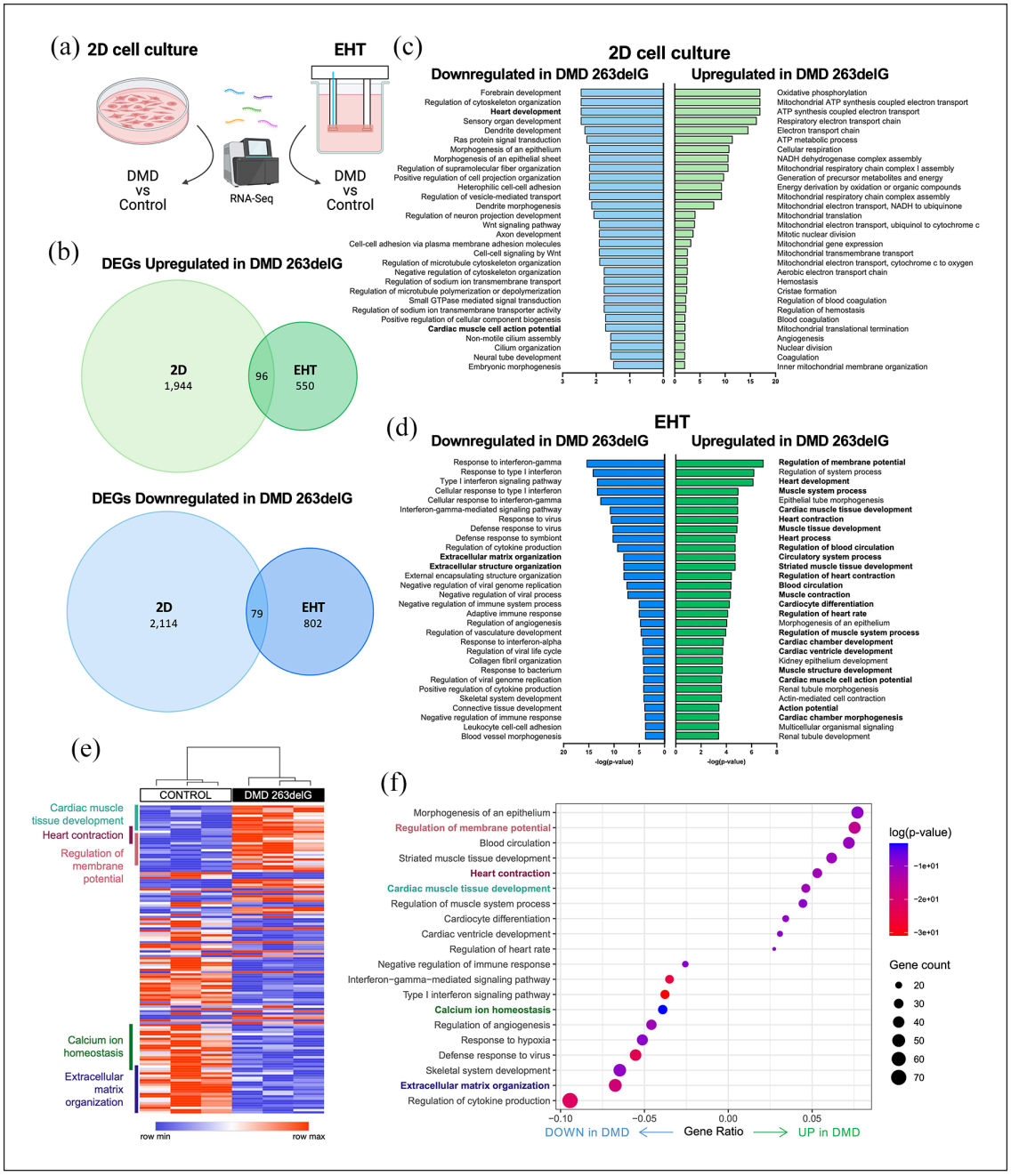

Figure 2. Transcriptome dysregulation in DMD 263delG hiPSC-CMs and EHTs. (a) Schematic of RNA-sequencing experiment where control and DMD 263delG hiPSC-CMs (7 weeks post differentiation) were compared and control and DMD 263delG EHTs (4 weeks post differentiation + 3 weeks EHT culture) were compared in separate experiments ($n = 3$). (b) Venn diagrams comparing the number of differentially expressed genes (DEGs) that were upregulated or downregulated in DMD 263delG 2D hiPSC-CMs and EHTs. (c) Top gene ontology (GO) processes up- or downregulated in DMD 263delG hiPSC-CMs and (d) EHTs, as ranked by p-value. GO terms relevant to cardiac biology appear in bold typeface. (e) Heatmap of a subset of normalized DEGs in control and DMD 263delG EHTs with hierarchical clustering represented by dendrogram ($n = 3$). Highlighted areas indicate genes corresponding to GO processes. (f) GO analysis of DEGs in DMD 263delG versus control EHTs.

significantly longer sarcomeres as compared to DMD 263delG EHTs (Figure 4(b)). However, we observed no significant difference in Z-disk width between control and DMD 263delG EHTs (Figure 4(c)). Additionally, it was observed that control and DMD 263delG EHTs had similar overall sarcomere alignment (Figure 4(d)). The observed shorter sarcomere spacing is consistent with the lower contractile forces observed in DMD 263delG EHTs.

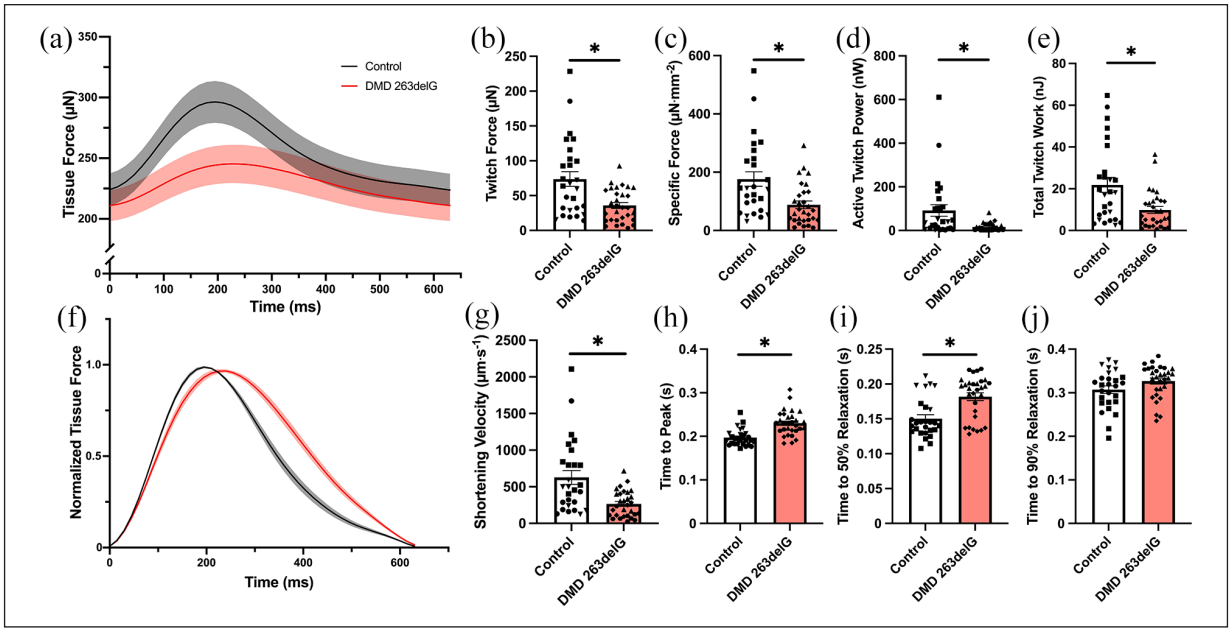

Figure 3. Auxotonic contractile properties of DMD 263delG EHTs. (a) Average tissue force traces of control and isogenic DMD 263delG EHTs. (b) Calculated maximum twitch force, (c) twitch stress, (d) active twitch power, (e) and total twitch work of EHT contraction. (f) Normalized average tissue force trace of control and isogenic DMD 263delG EHTs. (g) Calculated shortening velocity, (h) time to peak, (i) time to 50% relaxation, and (j) time to 90% relaxation. For (a and f), lines represent average ± S.E.M. Data shown represent all replicates from three independent experiments per cell line, different symbols represent different experimental batches (Control $n = 27$, DMD 263delG $n = 30$).

Altered Ca^{2+} transients in DMD EHTs

It was of interest to investigate the Ca^{2+} transients of dystrophic EHTs, as previous studies have pointed to Ca^{2+} dysregulation as a key phenotype of DMD presented in vitro.[22–25,28–31] To assess the extent of Ca^{2+} dysregulation in DMD 263delG EHTs, the ratiometric Ca^{2+} dye Fura-2 was used to assess both the kinetics of Ca^{2+} transients as well as the relative cytosolic Ca^{2+} levels under electrical field stimulation at 1.5 Hz. Comparing the ratiometric fluorescence intensities (Figure 5(a)) revealed significantly higher baseline levels of cytosolic Ca^{2+} (Figure 5(b)) as well as higher peak levels (Figure 5(c)) but with a decreased amplitude of Ca^{2+} flux in DMD 263delG EHTs (Figure 5(d)). Examining the kinetics of Ca^{2+} transients of control and DMD 263delG EHTs, normalized traces of cytosolic Ca^{2+} flux (Figure 5(e)) revealed slower time to Ca^{2+} transient peak in DMD 263delG EHTs (Figure 5(f)). We observed a decreased rate to 50% and 90% Ca^{2+} transient decay in DMD 263delG EHTs (Figure 5(g) and (h)). While we observed some batch-to-batch variability in measured 365 nm/380 nm values, the trends remained consistent. An examination of average force-Ca^{2+} loops highlighted the elevated Ca^{2+} level and decreased Ca^{2+} transient amplitude, as well as the decreased twitch force in DMD 263delG EHTs (Figure 5(i)). The significantly decreased force-Ca^{2+} loop area provided further evidence toward the lower Ca^{2+} flux as a significant contributor to the reduction of force seen in DMD 263delG EHTs (Figure 5(j)). All representative Ca^{2+} traces and images from Fura-2 measurement are shown in Supplemental Figure S6. These results point to elevated cytosolic Ca^{2+} and Ca^{2+} transient abnormalities as key contributors to the dystrophic phenotype presented in vitro.

Increased beat interval irregularity in DMD EHTs

To investigate consequences of Ca^{2+} transient abnormalities, we next investigated whether previously observed increased beat interval irregularity (ΔBI) was conserved in this model.[23,30] We found that DMD 263delG and control EHTs had similar average spontaneous beating frequencies (Figure 6(a)), but upon closer inspection of individual traces, intermittent irregular beats were observed to occur at a higher frequency in DMD 263delG EHTS (Figure 6(b)). We compared the difference between subsequent beat intervals ($\Delta BI = BI_{n+1} - BI_n$), which revealed a higher distribution of ΔBI in 263delG EHTs when distributions were compared with a nonparametric statistical test (Figure 6(c)). We noted that the distribution of ΔBI in the DMD 263delG EHTs spanned a greater time interval than the control EHTs. To highlight this difference, we selected a cutoff value of 1000 ms and compared the frequency with which ΔBI events exceeded this cutoff. This analysis revealed an increased occurrence of highly irregular events

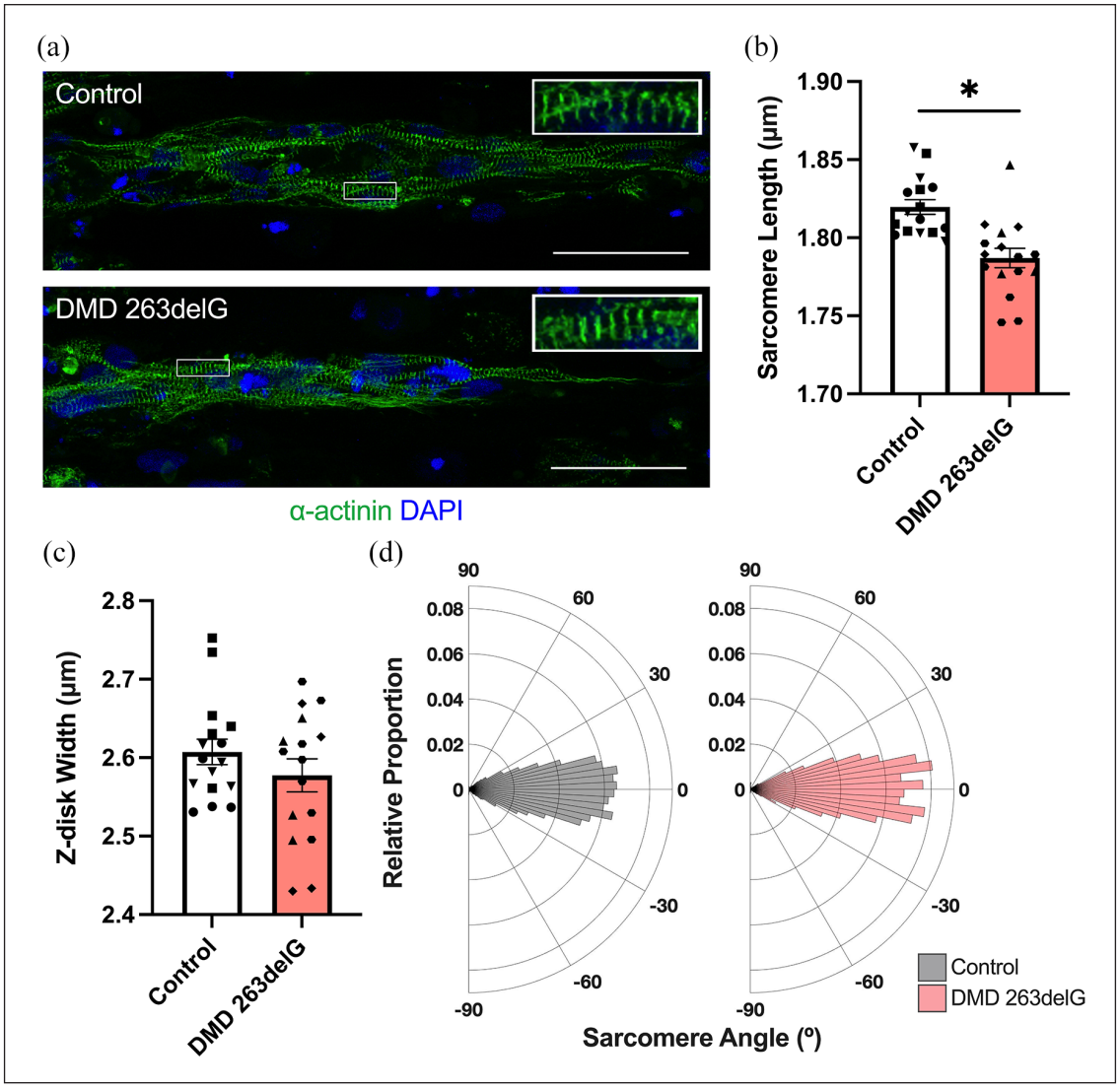

Figure 4. Sarcomere structure in DMD EHTs. (a) Representative control and DMD 263delG EHTs stained for α-actinin (green) and nuclei (blue) from which sarcomere measurements were made. Insets show a magnified view of striated sarcomeres. (b) Average measured sarcomere length and (c) Z-disk width from histological images of control and DMD 263delG EHTs. (d) Rose plots displaying distribution of sarcomere angles for all measured control and DMD 263delG EHTs ($n = 16$). Scale bars = 50 μm. Each data point represents an average of nine images for a single EHT. Data shown represent all replicates from three independent experiments, different symbols represent different experimental batches (Control $n = 16$, DMD 263delG $n = 16$).

in DMD 263delG EHTs (Figure 6(d)). All collected traces are shown in Supplemental Figure S7. These results indicate a potential downstream consequence of the altered Ca^{2+} transients observed in DMD 263delG EHTs.

Discussion

The mechanisms underlying cardiac disease initiation and progression in the absence of dystrophin are poorly understood, despite the prevalence of cardiomyopathy and heart failure as the leading cause of death for DMD patients. Thus, there is a need for human models of DMD to uncover the molecular drivers of cardiac pathology and to aid in the development of novel therapeutics. This is especially true considering recent unexpected adverse events and failure to meet clinical endpoints in several DMD gene therapy clinical trials currently underway.[51] Human-derived, 2D stem cell models have emerged as a powerful tool to study the disease characteristics of various *DMD* mutations and to test various pharmaceutical, gene editing, and exon skipping treatment approaches.[21] However, it is likely that 3D culture is needed to promote more physiological cell behavior and to better understand how the absence of full-length dystrophin affects tissue-level function. To address this, we developed a 3D tissue-engineered cardiac model of DMD and demonstrated that it recapitulates multiple key aspects of the disease (Figure 7).

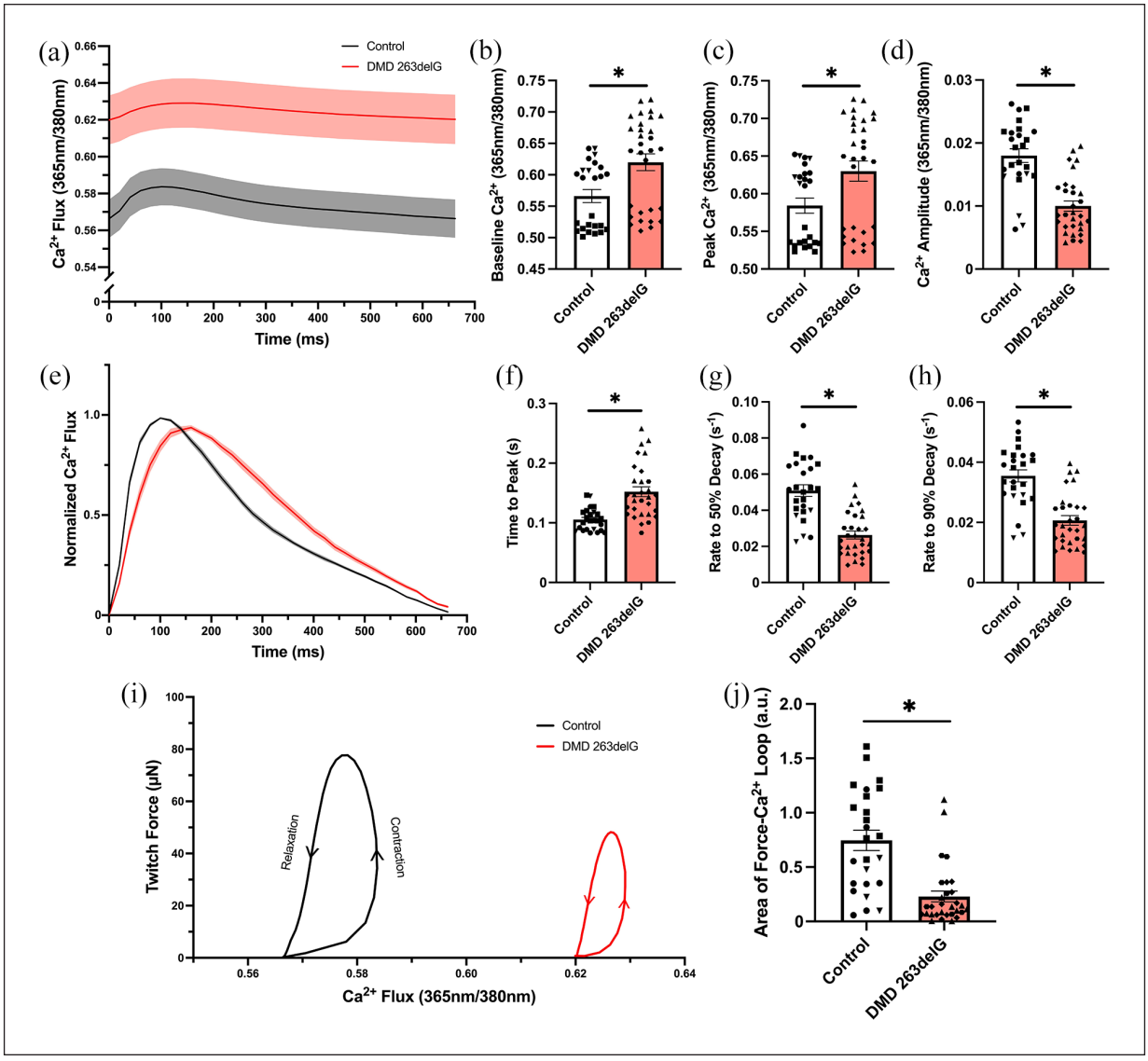

Figure 5. Ca^{2+} transients of DMD 263delG EHTs. (a) Average relative cytosolic Ca^{2+} levels during EHT contraction as measured with Fura-2 AM (365 nm/380 nm). (b) Measured baseline, (c) peak, and (d) amplitude of relative Ca^{2+} level. (e) Normalized average Ca^{2+} transient traces. (f) Calculated time to peak, (g) rate to 50% Ca^{2+} transient decay, and (h) rate to 90% transient decay. (i) Average force- Ca^{2+} loops of control and DMD 263delG EHTs. Twitch force and Ca^{2+} transients were simultaneously captured using the movement of the flexible post as seen with Fura-2 fluorescence. (j) Calculated area of force-Ca^{2+} loops (Control $n = 25$, DMD 263delG $n = 30$). For (a) and (e), lines represent average ± S.E.M. Data shown represent all replicates from three independent experiments per cell line, different symbols represent different experimental batches (Control $n = 25$, DMD 263delG $n = 30$).

We observed profound differences in transcriptomic changes that occur as a result of the DMD 263delG mutation in EHTs as compared to hiPSC-CMs grown in 2D culture. While both platforms produced clear transcriptomic differences between control and DMD 263delG genotypes, we found that the EHT platform evoked a smaller pool of transcriptional changes much more relevant to cardiac biology, highlighting the improved biological relevance of this 3D model. When comparing control and DMD 263delG EHTs, several biological processes of interest emerged during GO analysis, with which we can begin to hypothesize the molecular drivers of the dystrophic phenotype found in subsequent analysis of this model.

Dystrophin mutations have long been thought to cause myocyte frailty, although it is less understood how this affects cell contractility. In this study, we observed a decrease in auxotonic contractile performance in EHTs lacking full-length dystrophin. This finding is in agreement with previous studies performed on dystrophic hiPSC-CMs cultured as embryoid bodies,[30] as well as 3D engineered cardiac tissues under isometric loading.[25,52] This contractile deficit has also been observed in

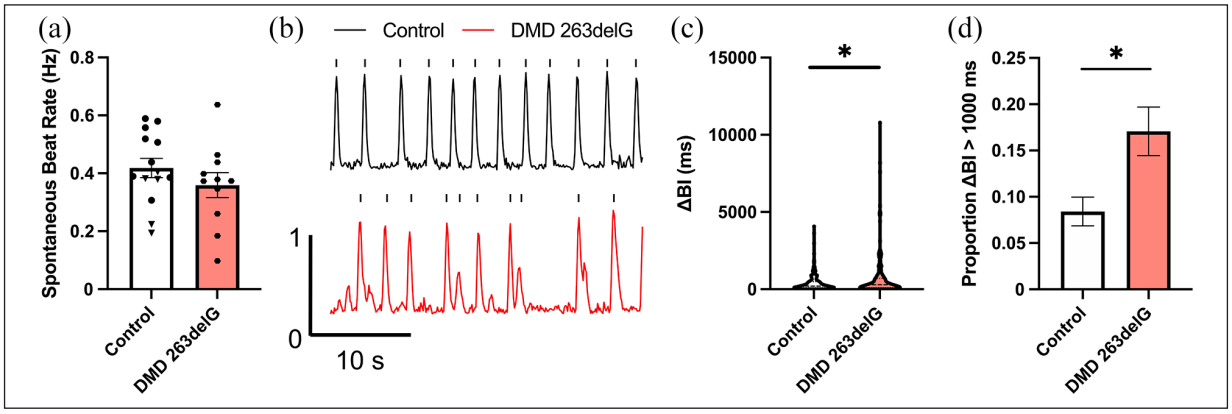

Figure 6. Spontaneous beat interval variability in DMD 263delG EHTs. (a) Spontaneous beat rate of control and DMD 263delG EHTs. (b) Representative traces of spontaneous EHT contraction with counted beats labeled with tick marks. (c) Distribution of calculated beat interval (BI) variability ($\Delta BI = BI_{n+1} - BIn$) measured over 30 s of spontaneous EHT contraction and (d) proportion of beats occurring with $\Delta BI > 1000$ ms. Data shown represent all replicates from 1 to 2 independent experiments, different symbols represent different experimental batches (Control $n = 14$, DMD 263delG $n = 11$).

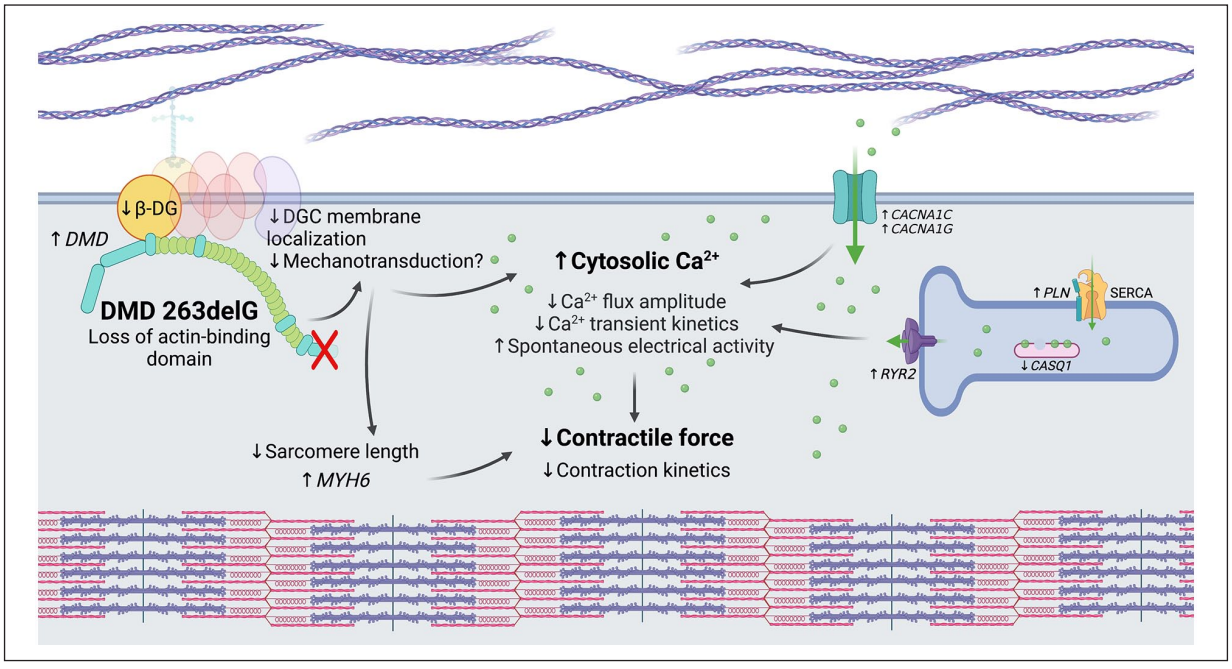

Figure 7. Summary of proposed mechanism of observed phenotypes in DMD 263delG EHTs.

myofibrils isolated from hiPSC-CMs lacking full-length dystrophin,[31] indicating that this phenotype is likely partially explained by changes at the sarcomere level. This notion is supported by our finding that while both control and DMD 263delG EHTs produced uniaxially aligned sarcomeres with similar Z-disk widths and sarcomere alignment, we found that DMD 263delG EHTs had significantly shorter sarcomeres. Regarding the kinetics of EHT contraction, we observed that dystrophic EHTs displayed slower force development as well as relaxation kinetics, in accordance with what has been observed at both the single cell and myofibril level, where isolated myofibrils from hiPSC-CMs lacking full-length dystrophin were found to have a slower fast phase of relaxation.[31] The delayed relaxation kinetics observed in this study replicate the diastolic dysfunction known to be one of the initial clinical phenotypes observed in patients with DMD.[53]

The contractile phenotype observed is further supported by our transcriptomic results, in which we observed upregulation of processes related to heart development and cardiomyocyte differentiation in DMD 263delG EHTs, including increased expression of *MYH6*, which has been shown to be a marker of hiPSC-CM immaturity and could also be a contributor to the observed decrease in

contractile forces.[54,55] DMD 263delG EHTs also displayed downregulation of genes related to extracellular matrix deposition and organization (several collagen genes, *MMP2*, *LOX*, *LOXL1*, *LOXL2*), which point to a potential inability of DMD 263delG hiPSC-CMs to exert their internal forces on the external environment, which could contribute to the observed decrease in EHT contractile forces.

Increased cytosolic Ca^{2+} levels and aberrant Ca^{2+} handling are thought to be key contributors to mechanisms of dystrophic pathology in patients. Here, for the first time, we examine the Ca^{2+} transients of dystrophin-mutant hiPSC-CMs in 3D culture, moving us closer toward understanding the role of dystrophin in mediating Ca^{2+} handling at the tissue level. We found that DMD 263delG EHTs had higher resting Ca^{2+} levels with a smaller amplitude of Ca^{2+} flux and delayed Ca^{2+} transient kinetics. Higher cytosolic Ca^{2+} [23,24,28] and slowed Ca^{2+} transient kinetics[22,25,29–31] have been previously observed in 2D cultured dystrophin-deficient hiPSC-CMs. It is thought that increased cytosolic Ca^{2+} in dystrophic myocardium can arise from multiple sources, including membrane tears[56] and stretch-activated channels,[57] and can be worsened by hyper-phosphorylation of Ca^{2+} channels[58] and a leaky sarcoplasmic reticulum due to increased ryanodine receptor open probability.[59] The observed increase in baseline cytosolic Ca^{2+} and decreased amplitude of Ca^{2+} flux in DMD 263delG EHTs are likely contributors to the observed contractile deficiencies and delayed contractile kinetics. As Ca^{2+} overload has been shown to mediate cardiac arrythmias[60,61] and previous studies have shown dystrophin-deficient hiPSC-CMs to have increased spontaneous beat rate variability,[23,27,30] we adapted a multi-electrode array method of assessing beat rate variability to assess arrhythmogenicity in this 3D model of DMD.[44] We observed that spontaneously contracting, dystrophic EHTs had a higher incidence of irregular beats, which we propose may be caused by the observed elevated cytosolic Ca^{2+}. To the best of our knowledge, this is the first time this dystrophic beat interval irregularity phenomenon has been observed in a 3D in vitro model.

The Ca^{2+} transient results are further supported by our transcriptomic data, which showed that DMD 263delG EHTs exhibited downregulation (*CASQ1*) and upregulation (*PLN*, *RYR2*) of genes related to sarcoplasmic reticulum function, which suggest decreased Ca^{2+} storage in the sarcoplasmic reticulum. Additionally, DMD EHTs displayed increased expression of genes related to excitation-contraction coupling and regulation of membrane potential (*SCN5A*, *CACNA1G*, *CACNA1C*), which could point toward membrane hyper-excitability and increased Na^{+} and Ca^{2+} currents causing prolongation of action potentials and increased incidence of early after depolarizations. Taken together, these results support the potential for electrophysiological remodeling that occurs as a consequence of, or as a compensatory mechanism in the absence of full-length dystrophin and thus help explain the observed elevated cytosolic Ca^{2+} levels, delayed Ca^{2+} transients, and increased beat rate variability.

Of note, it appears that sufficient cellular maturation may be required to expose this Ca^{2+} transient phenotype, as our group has found that dystrophic hiPSC-CMs displayed elevated Ca^{2+} levels, but only when exposed to a combination of maturational cues.[23] Additionally, others have observed that the elevated Ca^{2+} levels were exacerbated when dystrophic hiPSC-CMs were exposed to mechanical stretch.[28] These findings suggest that the EHT platform provides sufficient maturational cues and mechanical loading necessary to expose this Ca^{2+} transient phenotype that is thought to be central to DMD pathology. In this study, our specific DMD truncating mutation allows us to study the effect of protein structure on Ca^{2+} transients. Our model displays Ca^{2+} transient abnormalities despite retaining much of the dystrophin protein except for a portion of the actin-binding domain, illustrating a novel link between the mechanical cues provided by the full-length protein structure and Ca^{2+} handling. Additionally, this is the first time that a dystrophic Ca^{2+} handling defect has been shown in a 3D in vitro model, which is a significant step in advancing the clinical relevance of stem cell-derived disease models of DMD.

Studies in *mdx* mice have provided insight into mechanisms of DMD pathology, as they recapitulate some clinical aspects of DMD. While used extensively to study skeletal muscle pathology, the utility of this model to study dystrophic cardiomyopathy is greatly limited as this model displays few clinical signs of cardiomyopathy until old age or in the presence of multiple knockouts for dystroglycan complex proteins,[17] highlighting the need for humanized models of dystrophic cardiomyopathy. Our study revealed decreased force production with slowed kinetics in dystrophic EHTs. Similarly, a study performed with young *mdx* mice revealed decreased force production by isolated papillary muscles in addition to impaired myosin function as evidenced by in vitro motility.[14] Additionally, cardiomyocytes isolated from *mdx* mice display elevated cytosolic Ca^{2+}, although this phenotype only emerges in older mice (9–12 months),[4,62,63] whereas our EHT platform was able to recapitulate this finding in 3 weeks. It is intriguing to consider that a human model such as the one described herein may help in bridging the gap between animal models and clinical trials in the development of therapeutics to treat DMD.

This study has illustrated the power of a 3D in vitro model to recapitulate a variety of disease-relevant phenotypes in a single simple and highly tunable platform. To our knowledge, this is the first study to provide such an in-depth description of a hiPSC-derived dystrophic phenotype in a 3D, tissue-engineered model. In this EHT platform, the readout of force production provides a functional means by which to assess the extent of overall dystrophic cardiac dysfunction, as the observed Ca^{2+} dysregulation

and impaired sarcomere structure as well as unexplored potential deficiencies in mitochondrial function and nitric oxide signaling likely contribute to this observed reduction in contractile force. To this end, force production can be viewed as the integration of overall cardiac dysfunction, suitable for preclinical screening applications. Having established the disease phenotype presented in this study, future studies will be able to use this platform to more deeply investigate the mechanisms underlying DMD pathology and test emerging therapies in a physiologically-relevant platform. The contribution of Ca^{2+} overload to the contractile deficiencies in dystrophic EHTs can be investigated through the use of Ca^{2+} channel blockers or membrane sealants, as has been shown in previous in vitro studies.[23,24] Exon-skipping[26,64] and gene editing[29,65–67] have been shown to restore dystrophin expression in 2D hiPSC-CMs and limited studies have shown recovery of force of contraction in 3D engineered cardiac tissues,[25,52] but these studies have fallen short of describing a robust functional recovery in vitro. Through the studies described herein, we have made significant progress toward the development of a human-derived model of dystrophic cardiomyopathy.

Conclusions

Our ability to efficiently study DMD pathophysiology and develop emerging therapies is limited by the lack of functional *in vitro*, human disease models. In this study, we generated 3D human engineered heart tissue as a model of DMD and described the transcriptional changes and multifaceted disease phenotype presented. Stem cell-derived cardiomyocytes lacking full-length dystrophin, when cast into EHTs, were shown to display decreased force production and slowed kinetics, accompanied by decreased sarcomere lengths. For the first time, we examined Ca^{2+} transients in a 3D in vitro model of DMD and found that dystrophic EHTs had elevated baseline cytosolic Ca^{2+} levels with slowed Ca^{2+} release and reuptake. Lastly, we observed increased beat interval irregularity in dystrophic EHTs. Taken together, we present the value of a 3D tissue-engineered model of DMD in that it can replicate a variety of dystrophic phenotypes while providing a platform for assessment of overall cardiac function, something unattainable with most traditional tissue culture methods. Future studies will further uncover the mechanisms underlying the dystrophic phenotypes observed as well as explore the translational potential of this in vitro platform as a preclinical model of dystrophic heart disease.

Acknowledgements

This research was supported by the Cell Analysis Facility Flow Cytometry Shared Resource Lab in the Department of Immunology and the Garvey Imaging Core in the Institute for Stem Cell and Regenerative Medicine at the University of Washington. Select figures were created with BioRender.com.

Declaration of conflicting interests

The author(s) declared the following potential conflicts of interest with respect to the research, authorship, and/or publication of this article: N.J.S. and D.L.M. are scientific advisors and hold equity in Curi Bio, Inc. and D.L.M. is a founder of Kinea Bio, Inc. Other authors declare that no competing financial interests exist.

Funding

The author(s) disclosed receipt of the following financial support for the research, authorship, and/or publication of this article: This work was supported in part by the Institute for Stem Cell and Regenerative Medicine Innovation Pilot Award (to N.J.S. and D.L.M.), NSF CMMI-1661730 (to N.J.S.), NIH HL149734 (to N.J.S.), Senator Paul D. Wellstone Muscular Dystrophy Cooperative Research Center P50AR065139 (to D.L.M.), and the Jesse's Journey Foundation (to D.L.M.). Trainee support was provided by NIH/NIBIB grant T32EB001650 and the National Science Foundation Grant No. DGE-1762114 (to S.B.). Any opinions, findings, and conclusions or recommendations expressed in this material are those of the authors and do not necessarily reflect the views of the funding sources.

Research ethics and patient consent

This study involved no human or animal subjects.

Clinical trials

This study contains no clinical trials.

Reporting guidelines

This study involved no human or animal subjects.

ORCID iDs

Samantha B Bremner https://orcid.org/0000-0003-3465-0442
Ruby M Padgett https://orcid.org/0000-0002-9693-446X
J Manuel Pioner https://orcid.org/0000-0003-0179-3033

Supplemental material

Supplemental material for this article is available online.

Data

The RNA sequencing datasets described in this study can be accessed in the NCBI Gene Expression Omnibus (GEO) repository with accession ID GSE199242. Other datasets generated for this study are available from the corresponding author on request.

References

1. Eagle M, Baudouin SV, Chandler C, et al. Survival in Duchenne muscular dystrophy: improvements in life expectancy since 1967 and the impact of home nocturnal ventilation. *Neuromuscul Disord* 2002; 12: 926–929.
2. Rybakova IN, Patel JR and Ervasti JM. The dystrophin complex forms a mechanically strong link between the sarcolemma and costameric actin. *J Cell Biol* 2000; 150: 1209–1214.

3. Rapezzi C, Leone O, Biagini E, et al. Echocardiographic clues to diagnosis of dystrophin related dilated cardiomyopathy. *Heart* 2007; 93: 10–10.
4. Fanchaouy M, Polakova E, Jung C, et al. Pathways of abnormal stress-induced $Ca2^{+}$ influx into dystrophic mdx cardiomyocytes. *Cell Calcium* 2009; 46: 114–121.
5. Rohman MS, Emoto N, Takeshima Y, et al. Decreased mAKAP, ryanodine receptor, and SERCA2a gene expression in mdx hearts. *Biochem Biophys Res Commun* 2003; 310: 228–235.
6. Chang WJ, Iannaccone ST, Lau KS, et al. Neuronal nitric oxide synthase and dystrophin-deficient muscular dystrophy. *Proc Natl Acad Sci U S A* 1996; 93: 9142–9147.
7. Rando TA. Role of nitric oxide in the pathogenesis of muscular dystrophies: a "two hit" hypothesis of the cause of muscle necrosis. *Microsc Res Tech* 2001; 55: 223–235.
8. Khairallah M, Khairallah R, Young ME, et al. Metabolic and signaling alterations in dystrophin-deficient hearts precede overt cardiomyopathy. *J Mol Cell Cardiol* 2007; 43: 119–129.
9. Percival JM, Siegel MP, Knowels G, et al. Defects in mitochondrial localization and ATP synthesis in the mdx mouse model of Duchenne muscular dystrophy are not alleviated by PDE5 inhibition. *Hum Mol Genet* 2013; 22: 153–167.
10. van Westering T, Betts C and Wood M. Current understanding of molecular pathology and treatment of cardiomyopathy in Duchenne muscular dystrophy. *Molecules* 2015; 20: 8823–8855.
11. Shin J, Tajrishi MM, Ogura Y, et al. Wasting mechanisms in muscular dystrophy. *Int J Biochem Cell Biol* 2013; 45: 2266–2279.
12. Mora M, Di Blasi C, Barresi R, et al. Developmental expression of dystrophin, dystrophin-associated glycoproteins and other membrane cytoskeletal proteins in human skeletal and heart muscle. *Dev Brain Res* 1996; 91: 70–82.
13. Chevron MP, Girard F, Claustres M, et al. Expression and subcellular localization of dystrophin in skeletal, cardiac and smooth muscles during the human development. *Neuromuscul Disord* 1994; 4: 419–432.
14. Wagner S, Knipp S, Weber C, et al. The heart in Duchenne muscular dystrophy: early detection of contractile performance alteration. *J Cell Mol Med* 2012; 16: 3028–3036.
15. Górecki DC. Dystrophin: the dead calm of a dogma. *Rare Dis* 2016; 4: e1153777.
16. Bulfield G, Siller WG, Wight PA, et al. X chromosome-linked muscular dystrophy (mdx) in the mouse. *Proc Natl Acad Sci U S A* 1984; 81: 1189–1192.
17. McGreevy JW, Hakim CH, McIntosh MA, et al. Animal models of Duchenne muscular dystrophy: from basic mechanisms to gene therapy. *Dis Model Mech* 2015; 8: 195–213.
18. Pastoret C and Sebille A. Mdx mice show progressive weakness and muscle deterioration with age. *J Neurol Sci* 1995; 129: 97–105.
19. Chamberlain JS, Metzger J, Reyes M, et al. Dystrophin-deficient mdx mice display a reduced life span and are susceptible to spontaneous rhabdomyosarcoma. *FASEB J* 2007; 21: 2195–2204.
20. Yu X, Bao B, Echigoya Y, et al. Dystrophin-deficient large animal models: translational research and exon skipping. *Am J Transl Res* 2015; 7: 1314–1331.
21. Pioner JM, Fornaro A, Coppini R, et al. Advances in stem cell modeling of dystrophin-associated disease: implications for the wider world of dilated cardiomyopathy. *Front Physiol* 2020; 11: 368.
22. Guan X, Mack DL, Moreno CM, et al. Dystrophin-deficient cardiomyocytes derived from human urine: new biologic reagents for drug discovery. *Stem Cell Res* 2014; 12: 467–480.
23. Macadangdang JR, Miklas JW, Smith AST, et al. Engineered developmental niche enables predictive phenotypic screening in human dystrophic cardiomyopathy. *bioRxiv 456301*, 2018. DOI: 10.1101/456301.
24. Lin B, Li Y, Han L, et al. Modeling and study of the mechanism of dilated cardiomyopathy using induced pluripotent stem cells derived from individuals with Duchenne muscular dystrophy. *Dis Model Mech* 2015; 8: 457–466.
25. Kyrychenko V, Kyrychenko S, Tiburcy M, et al. Functional correction of dystrophin actin binding domain mutations by genome editing. *JCI Insight* 2017; 2: 1–16. DOI: 10.1172/jci.insight.95918
26. Sato M, Shiba N, Miyazaki D, et al. Amelioration of intracellular Ca^{2+} regulation by exon-45 skipping in Duchenne muscular dystrophy-induced pluripotent stem cell-derived cardiomyocytes. *Biochem Biophys Res Commun* 2019; 520: 179–185.
27. Eisen B, Ben Jehuda R, Cuttitta AJ, et al. Electrophysiological abnormalities in induced pluripotent stem cell-derived cardiomyocytes generated from Duchenne muscular dystrophy patients. *J Cell Mol Med* 2019; 23: 2125–2135.
28. Tsurumi F, Baba S, Yoshinaga D, et al. The intracellular Ca^{2+} concentration is elevated in cardiomyocytes differentiated from hiPSCs derived from a Duchenne muscular dystrophy patient. *PLoS One* 2019; 14: e0213768.
29. Moretti A, Fonteyne L, Giesert F, et al. Somatic gene editing ameliorates skeletal and cardiac muscle failure in pig and human models of Duchenne muscular dystrophy. *Nat Med* 2020; 26: 207–214.
30. Jelinkova S, Vilotic A, Pribyl J, et al. DMD pluripotent stem cell derived cardiac cells recapitulate in vitro human cardiac pathophysiology. *Front Bioeng Biotechnol* 2020; 8: 535.
31. Pioner JM, Guan X, Klaiman JM, et al. Absence of full-length dystrophin impairs normal maturation and contraction of cardiomyocytes derived from human-induced pluripotent stem cells. *Cardiovasc Res* 2020; 116: 368–382.
32. Bielawski KS, Leonard A, Bhandari S, et al. Real-time force and frequency analysis of engineered human heart tissue derived from induced pluripotent stem cells using magnetic sensing. *Tissue Eng Part C* 2016; 22: 932–940.
33. Leonard A, Bertero A, Powers JD, et al. Afterload promotes maturation of human induced pluripotent stem cell derived cardiomyocytes in engineered heart tissues. *J Mol Cell Cardiol* 2018; 118: 147–158.
34. Bremner SB, Goldstein AJ, Higashi T, et al. Engineered heart tissues for contractile, structural, and transcriptional assessment of human pluripotent stem cell-derived cardiomyocytes in a three-dimensional, auxotonic environment. In: Coulombe KLK and Black LD (eds) *Cardiac tissue engineering: methods and protocols*. New York, NY: Springer US, 2022, 2nd ed., pp. 87–97

35. Mihic A, Li J, Miyagi Y, et al. The effect of cyclic stretch on maturation and 3D tissue formation of human embryonic stem cell-derived cardiomyocytes. *Biomaterials* 2014; 35: 2798–2808.
36. Ruan JL, Tulloch NL, Razumova MV, et al. Mechanical stress conditioning and electrical stimulation promote contractility and force maturation of induced pluripotent stem cell-derived human cardiac tissue. *Circulation* 2016; 134: 1557–1567.
37. Ruan JL, Tulloch NL, Saiget M, et al. Mechanical stress promotes maturation of human myocardium from pluripotent stem cell-derived progenitors. *Stem Cells* 2015; 33: 2148–2157.
38. Abilez OJ, Tzatzalos E, Yang H, et al. Passive stretch induces structural and functional maturation of engineered heart muscle as predicted by computational modeling. *Stem Cells* 2018; 36: 265–277.
39. Shimko VF and Claycomb WC. Effect of mechanical loading on three-dimensional cultures of embryonic stem cell-derived cardiomyocytes. *Tissue Eng Part A* 2008; 14: 49–58.
40. Macadangdang J, Guan X, Smith AS, et al. Nanopatterned human iPSC-Based model of a dystrophin-null cardiomyopathic phenotype. *Cell Mol Bioeng* 2015; 8: 320–332.
41. Lian X, Zhang J, Azarin SM, et al. Directed cardiomyocyte differentiation from human pluripotent stem cells by modulating Wnt/β-catenin signaling under fully defined conditions. *Nat Protoc* 2013; 8: 162–175.
42. Sniadecki NJ and Chen CS. Microfabricated silicone elastomeric post arrays for measuring traction forces of adherent cells. *Methods Cell Biol* 2007; 83: 313–328.
43. Rodriguez AG, Han SJ, Regnier M, et al. Substrate stiffness increases twitch power of neonatal cardiomyocytes in correlation with changes in myofibril structure and intracellular calcium. *Biophys J* 2011; 101: 2455–2464.
44. Gilchrist KH, Lewis GF, Gay EA, et al. High-throughput cardiac safety evaluation and multi-parameter arrhythmia profiling of cardiomyocytes using microelectrode arrays. *Toxicol Appl Pharmacol* 2015; 288: 249–257.
45. Salick MR, Napiwocki BN, Kruepke RA, et al. The scanning gradient Fourier transform (SGFT) method for assessing sarcomere organization and alignment. *J Appl Phys* 2020; 127: 194701.
46. Liao Y, Smyth GK and Shi W. The R package rsubread is easier, faster, cheaper and better for alignment and quantification of RNA sequencing reads. *Nucleic Acids Res* 2019; 47: e47–e47.
47. Robinson MD, McCarthy DJ and Smyth GK. edgeR: a Bioconductor package for differential expression analysis of digital gene expression data. *Bioinformatics* 2010; 26: 139–140.
48. Wu T, Hu E, Xu S, et al. clusterProfiler 4.0: A universal enrichment tool for interpreting omics data. *Innovation* 2021; 2: 100141.
49. Banks GB, Gregorevic P, Allen JM, et al. Functional capacity of dystrophins carrying deletions in the N-terminal actin-binding domain. *Hum Mol Genet* 2007; 16: 2105–2113.
50. Gilbert G, Kadur Nagaraju C, Duelen R, et al. Incomplete assembly of the dystrophin-associated protein complex in 2D and 3D-cultured human induced pluripotent stem cell-derived cardiomyocytes. *Front Cell Dev Biol* 2021; 9: 737840.
51. Elangkovan N and Dickson G. Gene therapy for Duchenne muscular dystrophy. *J Neuromuscul Dis* 2021; 8: S303–S316.
52. Long C, Li H, Tiburcy M, et al. Correction of diverse muscular dystrophy mutations in human engineered heart muscle by single-site genome editing. *Sci Adv* 2018; 4: eaap9004.
53. McNally EM, Kaltman JR, Benson DW, et al. Contemporary cardiac issues in Duchenne muscular dystrophy. *Circulation* 2015; 131: 1590–1598.
54. Grancharova T, Gerbin KA, Rosenberg AB, et al. A comprehensive analysis of gene expression changes in a high replicate and open-source dataset of differentiating hiPSC-derived cardiomyocytes. *Sci Rep* 2021; 11: 15845. 111.
55. Aksel T, ChoeYu E, Sutton S, et al. Ensemble force changes that result from human cardiac myosin mutations and a small-molecule effector. *Cell Rep* 2015; 11: 910–920.
56. Petrof BJ, Shrager JB, Stedman HH, et al. Dystrophin protects the sarcolemma from stresses developed during muscle contraction. *Proc Natl Acad Sci U S A* 1993; 90: 3710–3714.
57. Yeung EW, Whitehead NP, Suchyna TM, et al. Effects of stretch-activated channel blockers on [Ca2$^+$]i and muscle damage in the mdx mouse. *J Physiol* 2005; 562: 367–380.
58. Wehrens XHT, Lehnart SE, Reiken SR, et al. Ca^{2+}/calmodulin-dependent protein kinase II phosphorylation regulates the cardiac ryanodine receptor. *Circ Res* 2004; 94: e61–e70.
59. Fauconnier J, Thireau J, Reiken S, et al. Leaky RyR2 trigger ventricular arrhythmias in Duchenne muscular dystrophy. *Proc Natl Acad Sci U S A* 2010; 107: 1559–1564.
60. Thandroyen FT, Morris AC, Hagler HK, et al. Intracellular calcium transients and arrhythmia in isolated heart cells. *Circ Res* 1991; 69: 810–819.
61. Schober T, Huke S, Venkataraman R, et al. Myofilament Ca sensitization increases cytosolic Ca binding affinity, alters intracellular Ca homeostasis, and causes pause-dependent Ca-triggered arrhythmia. *Circ Res* 2012; 111: 170–179.
62. Yasuda S, Townsend D, Michele DE, et al. Dystrophic heart failure blocked by membrane sealant poloxamer. *Nature* 2005; 436: 1025–1029.
63. Williams IA and Allen DG. Intracellular calcium handling in ventricular myocytes from *mdx* mice. *Am J Physiol Circ Physiol* 2007; 292: H846–H855.
64. Dick E, Kalra S, Anderson D, et al. Exon skipping and gene transfer restore dystrophin expression in human induced pluripotent stem cells-cardiomyocytes harboring dmd mutations. *Stem Cells Dev* 2013; 22: 2714–2724.
65. Zhang Y, Long C, Li H, et al. CRISPR-Cpf1 correction of muscular dystrophy mutations in human cardiomyocytes and mice. *Sci Adv* 2017; 3: e1602814.
66. Min YL, Li H, Rodriguez-Caycedo C, et al. CRISPR-Cas9 corrects Duchenne muscular dystrophy exon 44 deletion mutations in mice and human cells. *Sci Adv* 2019; 5: eaav4324.
67. Young CS, Hicks MR, Ermolova NV, et al. A single CRISPR-Cas9 deletion strategy that targets the majority of DMD patients restores dystrophin function in hiPSC-derived muscle cells. *Cell Stem Cell* 2016; 18: 533–540.